Journal of Materials Chemistry A

Efficient design and synthesis of an amorphous conjugated polymer network for a metal-free electrocatalyst of hydrogen evolution reaction

Journal:	*Journal of Materials Chemistry A*
Manuscript ID	TA-ART-10-2023-006447.R1
Article Type:	Paper
Date Submitted by the Author:	27-Dec-2023
Complete List of Authors:	Hamada, Wakana; Keio University Faculty of Science and Technology Graduate School of Science and Technology, Department of Applied Chemistry HISHIDA, MAFUMI; Tokyo University of Science Sugiura, Ryuto; Keio University Faculty of Science and Technology Graduate School of Science and Technology, Department of Applied Chemistry Tobita, Haruka; Keio University Faculty of Science and Technology Graduate School of Science and Technology, Department of Applied Chemistry Imai, Hiroaki; Keio University Faculty of Science and Technology Graduate School of Science and Technology, Department of Applied Chemistry Igarashi, Yasuhiko; Tsukuba Daigaku Oaki, Yuya; Keio University Faculty of Science and Technology Graduate School of Science and Technology, Department of Applied Chemistry

ARTICLE

Efficient design and synthesis of an amorphous conjugated polymer network for a metal-free electrocatalyst of hydrogen evolution reaction

Received 00th January 20xx,
Accepted 00th January 20xx

DOI: 10.1039/x0xx00000x

Wakana Hamada,[a] Mafumi Hishida,[b] Ryuto Sugiura,[a] Haruka Tobita,[a] Hiroaki Imai,[a] Yasuhiko Igarashi,[c] and Yuya Oaki*[,a]

Performances of functional polymers are enhanced by designing the structures in the different hierarchies, such as monomer, polymer, secondary structures, and nanoscale morphologies. In the present work, an amorphous conjugated polymer network was designed and synthesized to obtain a metal-free electrocatalyst for hydrogen evolution reaction (HER) in an efficient manner. A prediction model for the catalytic performance, *i.e.* overpotential for HER, was constructed using machine learning on small data based on the literatures. The straightforward liner prediction model assisted to design the network polymer containing quinone and heteroaromatic moieties. The simultaneous multiple reactions of benzoquinone (BQ) and benzoxazole (BO) formed the amorphous conjugated polymer network at 200 °C. After the morphology control, the BQ-BO polymer showed the overpotential 230 mV for electrochemical HER at 10 mA cm^{-2}, which is one of the highest performances in the metal-free electrocatalysts synthesized at low temperature. Moreover, we found that the amorphous conjugated polymer networks showed the specific hydration behavior in aqueous media. The results indicate that designing amorphous conjugated polymer network coupled with machine learning is a potential approach for development of functional materials.

Introduction

Assembly states of functional molecules have effects on the performances (Fig. 1a). For example, the functional molecules are assembled in main- and side-chain polymers, liquid crystals, metal-organic frameworks (MOFs), and covalent organic frameworks (COFs) to extract and enhance their performances.[1–9] Our group has proposed amorphous conjugated polymer network as a new type of the assembly states.[10–12] The specific structures have impact on the enhanced performances in energy-related applications.[10,11] The simultaneous reactions of the two or more monomers in multiple directions form the random network of the conjugated structures and their noncrystalline stackings as shown in Fig. 1b,c. The functional moieties are randomly dispersed in the network without the rigid aggregation as observed in the other crystalline assemblies (Fig. 1a). The noncrystalline stacking of the conjugated polymer network affords the flexibility related to the dynamic molecular motion. In addition, the nanostructured materials are formed by the dispersion and exfoliation in liquid phase because of the weak stackings. The improved performances are expected by these characteristic structures. In our previous report, the amorphous conjugated polymer network of BQ and pyrrole (Py) showed the HER catalytic performance.[11] In the present work, Py was changed to the other aromatic compounds containing oxygen, such as furan (Fu), benzofuran (BF), oxazole (Ox), and BO, because the hydrophilicity is a potential significant factor for the HER catalyst used in the aqueous phase. Therefore, the heteroaromatic compounds were selected based on the prediction of the catalytic performance, reactivity to BQ monomer, and hydrophilicity. The random copolymerization was achieved by BQ and BO via the simultaneous electrophilic substitution and pericyclic reaction (Fig. 1b,c). Moreover, the amorphous conjugated polymer networks containing BQ showed the specific hydration behavior by terahertz time-domain spectroscopy (THz-TDS).

Machine learning has been applied to exploration of new materials, optimization of processes, and enhancement of performances.[13–20] However, big data sufficient to machine learning is not always available particularly in conventional experiments in laboratory. Our group has studied sparse modeling for small data (SpM-S) to construct prediction models based on small data with combination of machine learning and chemical insights (Fig. 1d).[22–27] In SpM-S, the straightforward linear-regression model is prepared using a small number of the significant descriptors. The descriptors are first extracted using

[a] Department of Applied Chemistry, Faculty of Science and Technology, Keio University, 3-14-1 Hiyoshi, Kohoku-ku, Yokohama 223-8522, Japan. Email: oakiyuya@applc.keio.ac.jp
[b] Department of Chemistry, Faculty of Science, Tokyo University of Science, 1-3 Kagurazaka, Shinjuku, Tokyo 162–8601, Japan.
[c] Faculty of Engineering, Information and Systems, University of Tsukuba, 1-1-1 Tennodai, Tsukuba 305-8573, Japan.

† Footnotes relating to the title and/or authors should appear here.
Electronic Supplementary Information (ESI) available: [Experimental methods, Catalytic activity in previous works. Datasets. XPS, NMR, and UV-Vis spectra. Additional SEM and TEM analyses. Electrochemical properties.]. See DOI: 10.1039/x0xx00000x

machine learning and then selected with combining our chemical insight. Our method has advantages to construct prediction models based on small data compared with the other machine-learning algorithms.[24] In the present work, the method was applied to construct the overpotential (ΔE (>0)) predictor of metal-free HER catalyst. In general, Gibbs energy for adsorption of hydrogen on the catalyst (ΔG_{H^*}) is used as a metric of the activity.[28,29] However, ΔG_{H^*} of all the potential organic molecules is not easily calculated because of the high calculational cost. If the other metrics, such as ΔE and Tafel slope, are predicted in low calculation cost, the molecular design and synthesis can be accelerated to achieve the higher catalytic performance. Moreover, our SpM-S uses the descriptors with low calculation cost to construct the predictor.

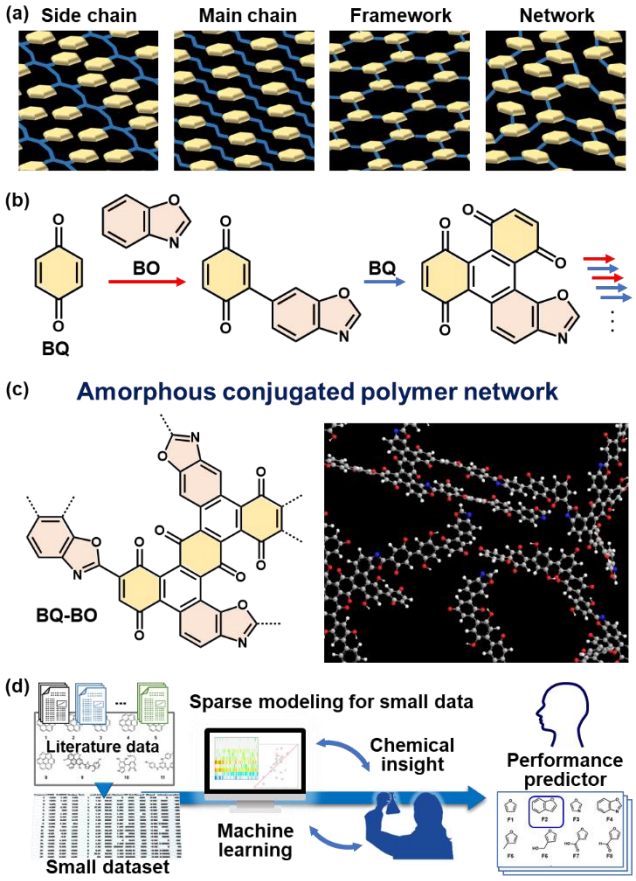

Fig. 1. Schematic illustration of designing a functional amorphous conjugated polymer network. (a) Models of side- and main-chain polymers, crystalline frameworks (MOFs and COFs), and conjugated polymer networks using hexagonal functional unit (yellow) and linker (blue). (b) Simultaneous multiple reactions of BQ and BO including the electrophilic substitution (red arrow) and pericyclic (blue arrow) reactions. (c) Unit structure and schematic illustration of the BQ-BO amorphous conjugated polymer network. (d) A general scheme of SpM-S for construction and application of the performance predictor combining machine learning and our chemical insight based on small data.

Hydrogen (H_2) is a promising clean energy source without emission of carbon dioxide (CO_2) during the use. Electrocatalyst is required for electrochemical HER, one of the efficient routes to produce H_2.[29–35] A variety of metal-free electrocatalysts, such as nanocarbons and COFs, have been studied as alternatives to platinum (Pt) and metal-based materials.[10,30,33,36–63] Here ΔE (at −10 mA cm^{-2}) and Tafel slope for electrochemical HER are summarized to compare the performances as the metal-free catalysts measured without the use of metal counter electrode (Fig. S1 and Table S1 in the Electronic Supplementary Information (ESI)).[36–58] The catalytic performance has been approached to that of Pt. For example, the heteroatom-doped nanocarbons showed ΔE lower than 150 mV on the curves of linear sweep voltammetry (LSV).[42,49,53] However, the synthetic temperature of the nanocarbons is generally higher than 800 °C (Fig. S1 and Table S1 in the ESI). Whereas H_2 is used to reduce the emission of CO_2, the high synthetic temperature of the catalysts contradicts the intention. ΔE = 207 and 220 mV were achieved using the graphitic caron nitride on graphene synthesized at 180 °C and the oxidized multi-walled carbon nanotubes treated at 120 °C, respectively.[41,52] However, these materials need the nanocarbons synthesized at high temperature. A recent report showed ΔE = 200 mV for the triazine-based COF synthesized at 150 °C for 72 h.[58] In the present work, the molecular design of a new metal-free electrocatalyst was conducted using an assistance of machine learning on the small data extracted from the literatures (Fig. 1d). The BQ-BO polymer was prepared by microwave-assisted synthesis at 200 °C for 1 h. After the morphology control, the HER catalytic activity was ΔE = 230 mV, which is one of the highest in the metal-free electrocatalysts prepared at low temperature (Fig. S1 and Table S1 in the ESI).[36–58]

Results and discussion

An overpotential predictor for metal-free HER catalyst.

A prediction model of ΔE was constructed based on small data collected from the literatures (Figs. 1d and 2 and Scheme S1 and Table S2 in the ESI).[11,38,49,55–63] The catalytic performances are changed by not only the molecular structures but also the other factors, such as assembly state, higher-ordered structures, and particle size. Herein, we assume that the factors other than the molecular structures are optimized to achieve the best performances in each previous report. The objective variable (y) was defined as the measured potential at −10 mA cm^{-2} ($y = P$ [mV] vs. RHE = $-\Delta E$) in the LSV curve, a standard metric for the catalytic performance. The data for 19 compounds (**1**–**19**), such as heteroatom-doped graphene and covalent organic framework, were collected from 12 literatures (Scheme S1 in the ESI).[11,38,49,55–63] When polymeric materials, such as graphene and COF, were used, the monomeric repeating units were extracted to calculate x_n (Scheme S1 in the ESI). Table 1 summarizes the explanatory variables (x_n: n = 1–11) as the potential descriptors: the energy levels of the highest occupied molecular orbital (HOMO) (E_{HOMO0}, x_1 / eV) and lowest unoccupied molecular orbital (LUMO) (E_{LUMO0}, x_2 / eV), the energy gap between HOMO and LUMO ($E_{g,HOMO\text{-}LUMO}$, x_3 (> 0) /eV), the number of the unoccupied orbitals (N_{orb} / –) with the energy level (E) lower than E = 0 (N_{orb}, $E_{LUMO0} \le E < 0$, x_4 / –), the sum of the absolute values of E within E_{LUMO0} and 0 ($\Sigma |E|$, $E_{LUMO0} \le E < 0$, x_5 / eV), polarizability (x_6 / 10^{40} C^2 m^2 J^{-1}), dipole moment (x_7 / Debye), Hansen solubility-(similarity-) parameter

(HSP) distance to water as the electrolyte solution (HSP distance, x_8 / –), the maximum and minimum values of the partial charge density (PCD_{max} and PCD_{min}, x_9 and x_{10} / –, respectively), the ratio of the number of the hetero atoms to the total number of atoms except hydrogen (R_{hetero}, x_{11} / –). These x_n (n = 1–11) were selected based on the following our chemical insights to study the effects of the molecular structures on ΔE: the reactivity of the redox reactions (x_n: n = 1–5), the charge distribution (x_n: n = 6, 7, 9, 10), the affinity to electrolyte solution (x_n: n = 8), and the effects of heteroatoms (x_n: n = 11). These values of the compounds **1**–**19** were calculated to prepare the training dataset.

Table 1 List of the explanatory variables (x_n: n = 1–11).

n / –	Explanatory variables x_n	Unit
1 [a]	E_{HOMO}	eV
2 [a]	E_{LUMO}	eV
3 [a]	$E_{g,HOMO-LUMO}$	eV
4 [a]	N_{orb}, $E_{LUMO0} \le E < 0$	–
5 [a]	$\Sigma\lvert E\rvert$, $E_{LUMO0} \le E < 0$	eV
6 [a]	Polarizability	10^{40} C^2 m^2 J^{-1}
7 [a]	Dipole moment	Debye
8 [b]	HSP distance	–
9 [a]	PCD_{max}	–
10 [a]	PCD_{min}	–
11 [c]	R_{hetero}	–

[a]Calculation values based on density function theory (DFT). [b]Calculation values based on Hansen solubility (similarity) (HSP) parameters. [c]Calculation value based on the molecular structure.

The overpotential predictor was constructed by SpM-S using the small dataset (Fig. 2).[22] Exhaustive search for linear regression (ES-LiR) was carried out using the dataset containing 19y and x_n (n = 1–11) to visualize the contribution of each x_n in the weight diagram (Fig. 2a). After the linear regression models were exhaustively prepared by all the combinations of x_n, *i.e.* 2^{11}–1 (= 2047) patterns except the case that no descriptors are selected, the models were sorted in the ascending order of cross validation error (CVE) values. Cross-validation is a technique for evaluating a machine learning model and approximately estimating prediction accuracy from a limited amount of data. Leave-one-out cross-validation was used in the present study. Their positive and negative coefficients of the used descriptors were visualized by the warm and red colors in the weight diagram, respectively (Fig. 2a). The densely colored x_n means the frequently extracted descriptors. The warmer and cooler colors imply the stronger contribution to y. Three descriptors x_7, x_9, and x_{10} were selected by the combination of the weight diagram and our chemical insight. The linear regression model eqn (1) was constructed to estimate the predicted y (y') using three descriptors with the coefficients converted to the normalized frequency distribution (mean 0 and standard deviation 1).

$$y' = 42.00x_7 + 48.69x_9 - 48.97x_{10} - 344.5 \quad \ldots (1)$$

The relationship between the estimated and measured overpotentials (y'-y) had root mean squared error (RMSE) 121.0 mV for the training dataset (Fig. 2b). The average RMSE was 118 ± 12.7 mV for the training and 144 ± 118 mV for the test in ten-fold cross validation using the dataset (Fig. S2 in the ESI), supporting the validity of the selected descriptors. Although the predictor is a simple linear regression using three descriptors, ΔE of new compounds can be estimated using eqn (1). The positive correlations of x_7 (dipole moment) and x_9 (maximum of the partial charge density) and negative correlation of x_{10} (minimum of the partial charge density) imply that the more charge-localized state in the molecule facilitates adsorption of proton to promote HER. In 15 compounds with the predicted ΔE lower than 400 mV, 11 compounds actually showed ΔE lower than 400 mV (the dashed lines and arrows in Fig. 2b). Although the accuracy 73.3 % is not so high, the predictor can be used as a simple guideline to estimate ΔE with low calculation cost. In the present work, the predictor was used for the molecular design of amorphous conjugated polymer networks. Professional chemists have their own empirical design strategies of molecules for the catalysts in brain. The fact means that the specific parameters related to the catalytic performance, *i.e.* the descriptors, are not elucidated for the other chemists. In the present work, machine learning assists the construction of the linear regression model eqn (1) comprising of the specific descriptors and their coefficients. The model represents the corelated parameters and their weights to the catalytic performance. The straightforward predictor can assist the further design and exploration of new potential molecules for HER catalysts by not only our group but also the other researchers

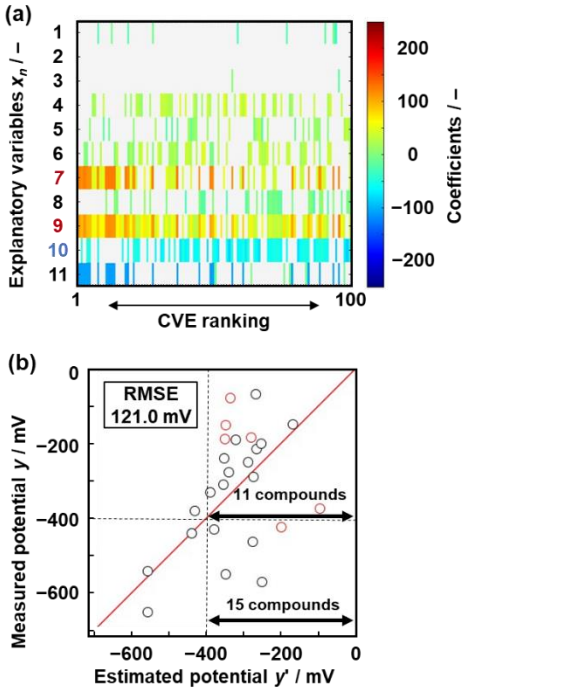

Fig. 2. SpM-S for construction of the prediction model. (a) Weight diagram representing the coefficients of each x_n in the constructed models with the

ascending order of CVE values (the smallest 100). (b) Relationship between the estimated and measured (reported) potential (−Δ*E*: black and red circles for the training and test data, respectively).

New compounds **20**–**25** that were not used in the training data were collected from the literatures (Scheme S2 and Table S2 in the ESI).[64–68] The relationship between the predicted and reported values was studied using the test data to validate the prediction model (the red circles in Fig. 2b, RMSE 211 mV). As all these six catalysts showed predicted Δ*E* lower than 400 mV, the five compounds had the actual Δ*E* lower than 400 mV. The accuracy is calculated to be 83.3 %, which is not different from 73.3 % for the training data. The results imply that the predictor is used for the exploration of new potential HER catalysts. The precise Δ*E* is not predicted because of the calculation based on the simple model and unit molecular structure. The model can be used to screening the new potential compounds.

Molecular design of amorphous conjugated polymer networks containing quinone moiety.

In our previous work, the amorphous conjugated polymer network of BQ and Py was applied to the electrocatalyst.[11] Our intention here is to find another heteroaromatic compound instead of Py for enhancing the catalytic activity. The BQ-based copolymer was designed using commercially available furan and oxazole derivatives furan (Fu), benzofuran (BF), oxazole (Ox), BO and **F1**–**F10** because of the potential hydrophilicity as mentioned later (Scheme 1). BQ was virtually reacted with Fu, BF, Ox, BO, and **F1**–**F10** to form the diads on the assumption of electrophilic substitution (Fig. 1b and Scheme 2). The Δ*E* of the prepared 14 diads was predicted using the model eqn (1). The predicted Δ*E* (ΔE_{pred}) of these diads were lower than 410 mV and the average was 368 mV (Table 2). For example, the virtually generated diads showed ΔE_{pred} = 410 mV for BQ-Fu, 364 mV for BQ-BF, 400 mV for BQ-Ox, and 356 mV for BQ-BO. As the accuracy of the predictor was around 70 % for the compounds with ΔE_{pred} < 400 mV, the prediction results imply the potentials of the furan and oxazole derivatives. In addition, the hydrophilicity of the furan derivatives is also an important factor to improve the catalytic performance because the catalyst is used in aqueous phase. The HSP distances of the diads based on the furan derivatives to water were calculated to be 10.8 for BQ-Fu, 11.2 for BQ-BF, 10.8 for BQ-Ox, and 11.1 for BQ-BO. These values were smaller than those of the diads based on Py and thiophene (Tp), such as 12.5 for BQ-Py and 12.6 for BQ-Tp. The smaller HSP distance indicates the higher affinity to the solvent. In this manner, furan derivatives were selected based on the prediction of the catalytic performance and hydrophilicity.

The synthetic experiment was performed using the furane derivatives with the simple structures, namelyFu, BF, Ox, and BO, to study the reactivity for the polymerization because the reactivity is not predicted by the model at the present state.

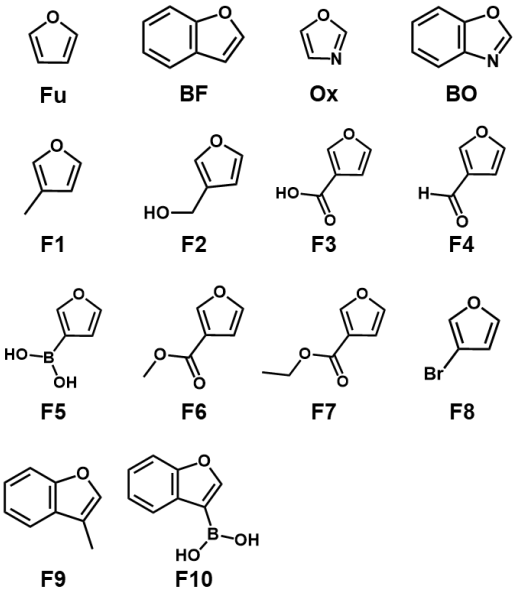

Scheme 1. Molecular structures of Fu, BF, Ox, BO, and **F1**–**F10** for the virtual generation of the diads with BQ.

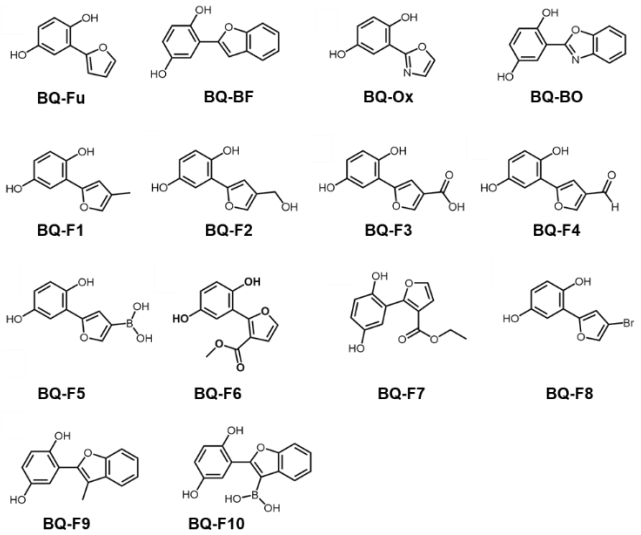

Scheme 2. Molecular structures of the virtually generated diads based on BQ and furane derivatives Fu, BF, Ox, BO, and **F1**–**F10**.

Table 2. Predicated Δ*E* of the diads based on BQ and furane derivatives.

BQ-	FU	BF	Ox	BO	F1	F2	F3	F4	F5	F6	F7	F8	F9	F10
Δ*E* / mV	410	364	400	356	404	387	344	358	363	288	334	387	397	355

Δ*E* of the virtually prepared diads in Scheme 2 were calculated using the prediction model eqn (1).

BQ powder and the heteroaromatic compounds (Fu, BF, Ox, and BO) were mixed and then reacted under the microwave irradiation without addition of solvents at 170 °C for Fu and Ox and 200 °C for BF and BO for 1 h. The resultant materials were purified under vacuum condition at 190 °C for 16 h to remove the remaining monomers and oligomers. The detailed procedure was described in the ESI. The BQ-BO polymer with the black color was obtained with the average yield 13.3 %. In contrast, the polymerization products were not obtained for Fu, BF, and Ox with the sufficient yields.

Structures of the BQ-BO amorphous conjugated polymer network.

The resultant BQ-BO polymer showed the weight loss in the range of 400 to 600 °C originating from the combustion in thermogravimetry (TG) analysis under air atmosphere (Fig. 3a). The weight loss was observed in the higher temperature range compared with that of the monomeric BQ and BQ-hydroquinone (HQ) charge-transfer complex (BQ-HQ). The temperature range of the weight loss was higher than that of a commercial polypyrrole (PPy) and similar to that of a commercial graphene oxide (GO). The TG analysis implies the formation of not the chain-like but the network polymer. When the resultant BQ-BO was dried at 60 °C for 6 h, the weight loss was observed in the range of 150–400 °C. The fact indicates that the removal of the remaining low-molecular-weight contents from the resultant polymer requires vacuum drying at 190 °C for 6 h.

The absorptions corresponding to O–H, C–H, C=O, C=C, C=N, and C–O–C were observed in the Fourier-transform infrared (FT-IR) spectrum as follows (Fig. 3b,c): O–H stretching vibration (A), C–H stretching vibration (B), C=O stretching vibration (C), C=C stretching vibration (D), both C=N and C–O–C stretching vibrations (E, overlapped). The estimated structural units of BQ-BO have these bonds (Fig. 3c). In addition, the related bonds were detected in C1s, O1s, and N1s peaks of X-ray photoelectron spectroscopy (XPS) (Fig. S3 in the ESI). The formation of the estimated polymer network was supported by solid-state ^{13}C nuclear magnetic resonance (NMR) spectroscopy (Fig. S4 in the ESI). The weight ratio of C, H, N, and O (others) was measured to be 67.0 : 3.1 : 2.7 : 27.1 by elemental analysis. Based on the weight ratio, Fig. 3d shows the repeating units and their molar ratio. The units include 48 % of the HQ moiety as the reduced state of BQ. The composition of the estimated structure was calculated to be C : H : N : O = 67.1 : 2.8 : 2.6 : 27.5. The measured and calculational compositions were consistent with each other within 0.5 %. These structural analyses indicate the formation of the BQ-BO network polymer, as shown in Fig. 1c.

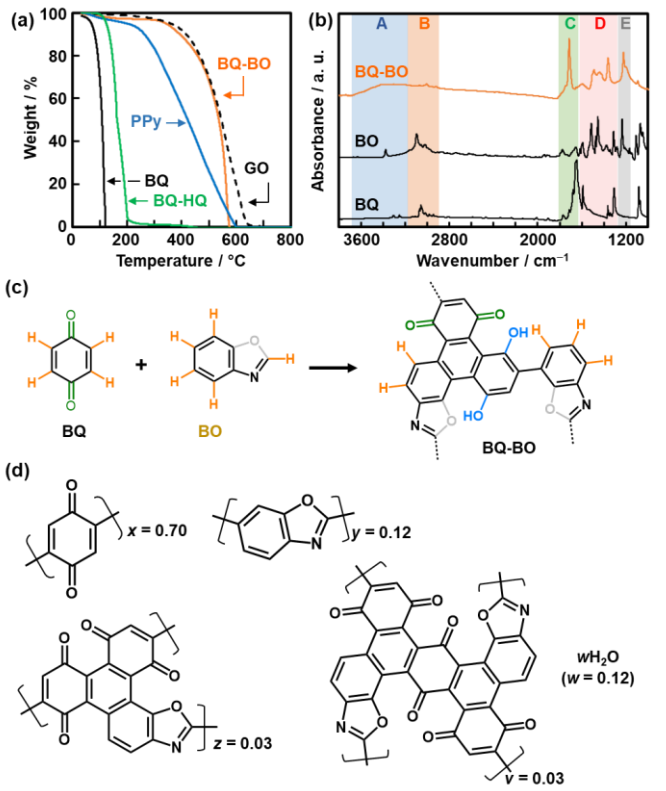

Fig. 3. Structural analyses of BQ-BO. (a) TG curves of BQ-BO (orange), BQ (black), BQ-HQ charge-transfer complex (green), PPy (blue), and GO (dashed line). (b) FT-IR spectra of BQ-BO (top), BQ (middle), and BO (bottom). (c) Molecular structures of the monomers and BQ-BO oligomeric unit. (d) Composition of the repeating units in BQ-BO.

The G and D bands characteristic of graphitic structure and its defect were observed at 1350 and 1580 cm^{-1} in the Raman spectrum, respectively (Fig. 4a). The peaks were broadened compared with those of a commercial glassy carbon (GC) and GO. UV-Vis-near infrared (NIR) spectrum of the BQ-BO polymer showed the absorption in the range of 200 to 1800 nm (Fig. S5 in the ESI), whereas the charge-transfer complex of BQ-HQ had the absorption edge around 800 nm. The Raman and UV-Vis spectra indicate that BQ-BO contains the extended conjugated structure like a graphitic network.

In this manner, an increase in the molecular weight was supported by TG-DTA. The functional groups in the polymer network were analyzed by FT-IR. The XPS and NMR analyses indicates the inclusion of all the chemical bonds in the estimated network structure as shown in Fig. 3d. In addition, formation of the π-conjugated network structures is supported by the UV-Vis-NIR and Raman spectra. Fig. 3d shows one of the possible structures consistent with all these analytical results.

The broadened and weak halo was observed around 2ϑ = 25 ° on the X-ray diffraction (XRD) pattern (Fig. 4b). Commercial GO, GC, and graphene (reduced GO) showed the peaks corresponding to the stacking of the graphitic layers around 2ϑ = 25 °. The diffraction of BQ-BO was weaker and broader than that of the references. The XRD analysis indicates that the BQ-BO conjugated polymer network forms the low-crystalline stacking.

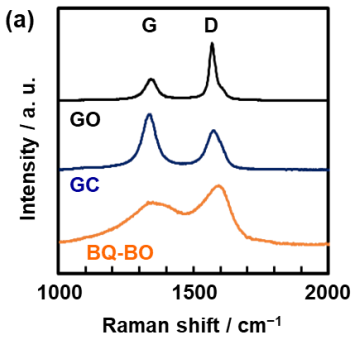

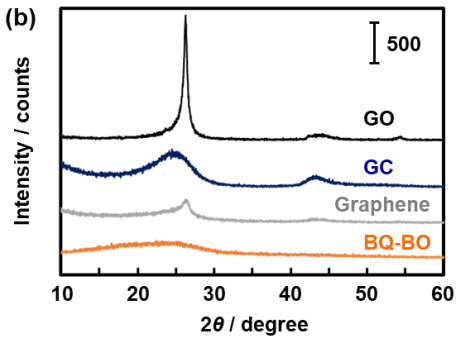

Fig. 4. Raman spectra (a) and XRD patterns (b) of BQ-BO and its reference commercial nanocarbons.

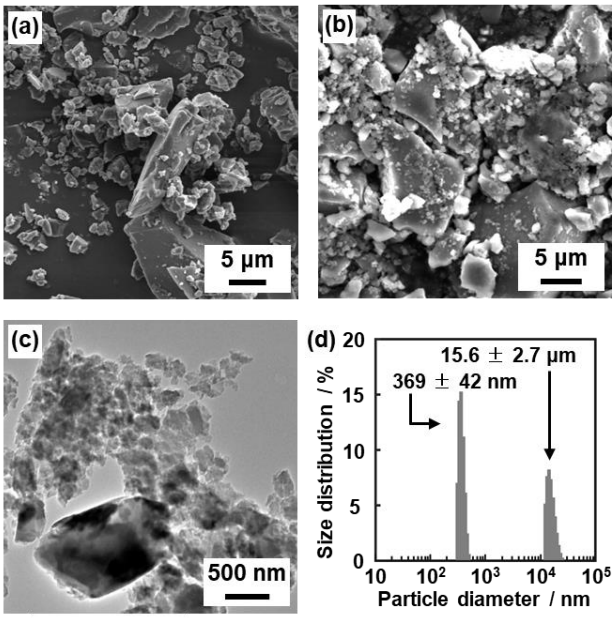

Fig. 5. Morphology and particle size of BQ-BO. (a,b) SEM image of the BQ-BO bulk (a) and bulk-nano sample after the dispersion in acetone (b). (c,d) TEM image (c) and DLS particle-size distribution (d) of BQ-BO dispersed in acetone.

The irregularly shaped BQ-BO particles 1–50 μm in size were observed on the images of scanning electron microscopy (SEM) (Fig. 5a and Fig. S6 in the ESI). These bulk particles were dispersed in organic media, such as acetone and ethylbenzene, under ultrasonication. The size of the bulk particle reduced less than 20 μm in size after the dispersion (Fig. 5b and Fig. S7 in the ESI). In addition, the nanoparticles smaller than 500 nm in size appeared in addition to the original bulk particles on the SEM and transmission electron microscopy (TEM) images (Fig. 5b,c and Fig. S7 in the ESI). The energy-dispersive X-ray (EDX) analysis implies that each BQ-BO particle contained C, N, and O (Figs. S6 and S7 in the ESI). The BQ-BO particles showed no diffraction rings in the selected-area diffraction (SAED) pattern and lattice fringes in the high-resolution TEM (HRTEM) image (Fig. S8 in the ESI), supporting the amorphous nature of BQ-BO. The BQ-BO samples including the bulk and nanoparticles (bulk-nano) after the dispersion in acetone contained C, N, and O components without the other elements in the EDX analyses of the SEM and TEM observations (Fig. S8 in the ESI). The dissolution and/or exfoliation generate the smaller particles. Two peaks were observed on the particle-size distribution by dynamic light scattering (DLS) (Fig. 5d). The dispersion liquid containing bulk and nanoparticles (bulk-nano) were used to prepare the electrode for HER (Fig. 6).

HER catalytic performances of BQ-BO.

The dispersion liquid containing the mixture of the bulk and nanoparticles was dropped on a commercial GC electrode (Fig. 5b,c). The bulk BQ-BO particles before the dispersion was used as the reference sample (Fig. 5a). The GC electrode loading the BQ-BO sample, graphite rod, and Ag/AgCl electrode were used as the working, counter, and reference electrodes, respectively. The electrodes were set in a twin-beaker cell with 0.5 mol dm^{-3} sulfuric acid (H_2SO_4) as the electrolyte.

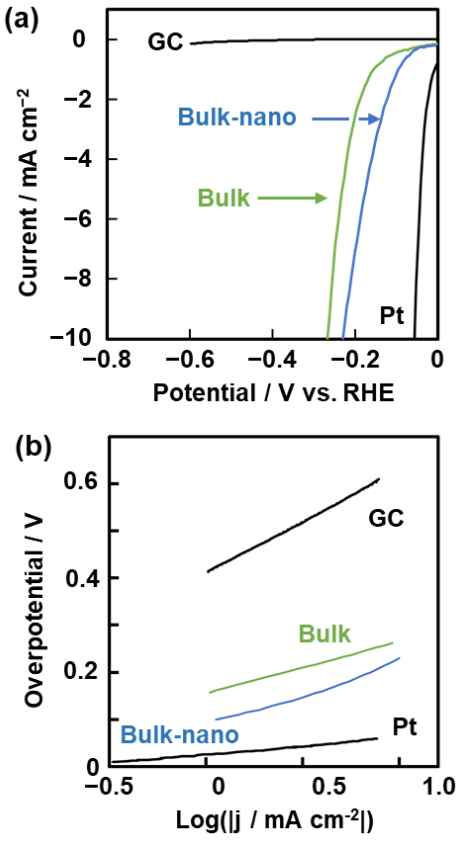

Fig. 6. LSV curves (a) and Tafel slopes (b) of the bulk (green) and bulk-nano (blue) BQ-BO samples and reference Pt and GC (black).

Cyclic voltammetry (CV) showed the broadened redox peaks corresponding to the anthraquinone (AQ) and BQ moieties around −0.1 and 0.7 V vs. RHE (RHE: −0.199 V vs. Ag/AgCl), respectively (Fig. S9 in the ESI). The presence of the AQ and BQ moieties is consistent with the estimated structure in Fig. 1c. Chronoamperometry (CA) was performed at −0.3 V vs. RHE for 5 h to reduce the BQ moiety to HQ state with recovering the π conjugation in the network (Fig. S9 in the ESI). Then, the HER electrocatalytic activity was measured by LSV in the range of 0 and −0.6 V (vs. RHE) at 5 mV s^{-1} (Fig. 6a). The bulk-nano BQ-BO sample showed ΔE = 230 mV (at −10 mA cm^{-2}) (Fig. 6a), whereas ΔE of the bulk BQ-BO was 279 mV. The catalytic performance of the bulk-nano BQ-BO was reproducible for the five different samples (Fig. S6 in the ESI). The Tafel slope, representing the kinetics of HER, was 138 mV dec^{-1} for the bulk-nano and 190 mV dec^{-1} for the bulk samples (Fig. 6b). ΔE of the bulk-nano BQ-BO was one of the smallest values in the metal-free electrocatalysts synthesized lower than 200 °C (Fig. S1 in the ESI).[11,38,49,55–63]

The enhanced HER performance is achieved by the specific morphologies and molecular structures. The nanostructures with the BQ-BO bulk particle contribute to an increase in the specific surface area for the catalytic reaction. The bulk particles ensure the large interspace for diffusion of the electrolyte solution without the dense aggregation of the nanoparticles. The electrochemical double-layer capacitance (C_{dl}) of the BQ-BO bulk-nano sample was estimated to be 4.3 mF cm^{-2} from the cyclic voltammograms (Fig. S9 in the ESI). The C_{dl} value was comparable to the other HER catalysts based on various nanocarbons with the graphitic structures, such as C_{dl} = 2.4,[37] 3.6,[53] 5.0,[54] and 2.2 mF cm^{-2},[57] in previous works, although the larger values, such as 22.3[53] and 24.4 mF cm^{-2},[54] was observed for the more porous structures. These facts imply that the enhanced electrochemical surface area of the BQ-BO bulk-nano particles is derived from the specific morphology. In addition, the BQ-BO polymer network has the suitable structures in molecular level. The conductivity is derived by the conjugated structures. The charge transfer resistance (R_{ct}) was measured to be 90.9 Ω even for the bulk BQ-BO particles before the dispersion in acetone by electrochemical impedance spectroscopy (EIS) (Fig. S9 in the ESI). R_{ct} in the same order of magnitude was reported in the previous works about the metal-free HER catalysts.[61,69] The BQ-BO polymer has the sufficient conductivity for the HER reaction.

The heteroatoms, such as N and O, play important roles for the generation of the active sites. DFT calculation was performed to study the active sites as electrocatalyst. In previous works, the Gibbs energy for the hydrogen adsorption (ΔG_{H^*}) is regarded as a significant parameter related to the HER catalytic activity on the metal surfaces.[70,71] When the value of the calculated ΔG_{H^*} is positive and negative, the rate determining step is formation of the intermediate adsorbed hydrogen (H*) on the surface and desorption of H* to generate H_2, respectively. The higher activity is achieved by the catalysts with the smaller absolute value of ΔG_{H^*} ($|\Delta G_{H^*}|$). In recent years, the calculational study is applied to not only metals but also metal-free HER catalysts.[36–38,58,59,61,69,72] In the present work, the active sites with the smaller $|\Delta G_{H^*}|$ were explored in the unit structure of BQ-BO (Fig. 7). Coronene was used as a reference structural unit of graphitic carbon without containing heteroatoms (Fig. 7a). ΔG_{H^*} was calculated to be 2.21 eV for adsorption of H* on the plane of sp^2 carbon (the site 0 in Fig. 7a). The BQ-BO polymer showed ΔG_{H^*} smaller than 1.5 eV on the neighboring carbons of the heteroatoms (the sites 1, 2, 4, and 6 in Fig. 7b), whereas ΔG_{H^*} larger than 3.0 eV was calculated with the direct adsorption of H* on the heteroatoms. Although the $|\Delta G_{H^*}|$ values themselves are not so small compared with those of the other metal-free HER catalysts in the previous works, the neighboring carbons of the heteroatoms with $|\Delta G_{H^*}|$ lower than that of the inert sp^2 carbon can act as the potential active sites. The results imply that the BQ-BO polymer has the larger amount of the active sites homogenously distributed in the network structure. Moreover, the BQ and HQ moieties have effects on the hydrophilicity in aqueous phase. In this manner, the enhanced HER catalytic performance is achieved using the BQ-BO polymer.

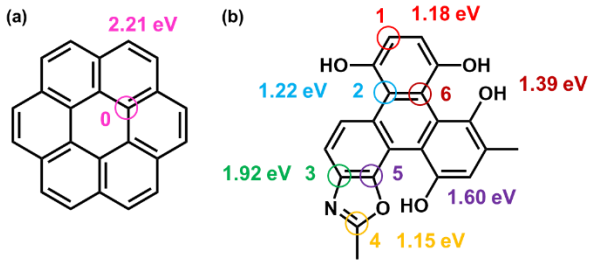

Fig. 7. ΔG_{H^*} on the sites 0 (a) and 1–6 (b) estimated by DFT calculation. (a) A simplified model for graphitic carbon without any heteroatoms as a reference. (b) Unit structure of BQ-BO polymer with the potential active sites 1–6.

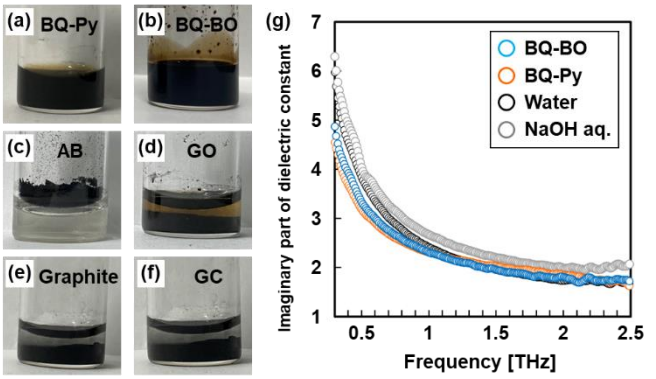

Fig. 8. Hydration state of the amorphous conjugated polymer networks. (a–f) Photographs of BQ-Py (a), BQ-BO (b), AB (c), GO (d), graphene (e), and GC (f) dispersed in NaOH aq. (g) Imaginary part of the dielectric constants in THz frequency region of purified water, NaOH aq, and dispersion liquids containing BQ-BO and BQ-Py in 1mol dm^{-3} NaOH.

Hydrophilicity of the amorphous conjugated polymer networks.

Here we found the specific hydrophilicity of the amorphous conjugated polymer networks. Hydrophilicity can be a potential factor related to the enhanced HER catalytic performance in

aqueous phase. The dispersibility and hydration behavior of the BQ-BO polymer in aqueous phase was compared with those of typical carbon materials, such as commercial acetylene black (AB) carbon, GO, graphite, and GC (Fig. 8). In addition, the BQ-Py polymer in our previous work was used as another sample.[11] The powder of BQ-BO, BQ-Py, AB, GO, graphite, and GC, was dispersed in 1 mol dm^{-3} sodium hydroxide (NaOH) aqueous solution at the concentration 10 wt%. Interestingly, BQ-BO and BQ-Py were dispersed in the NaOH solution (Fig. 8a,b). In contrast, the other reference carbons were immiscible and segregated from the aqueous phase (Fig. 8c–f). The photographs imply the specific affinity of BQ-BO and BQ-Py to aqueous phase.

The hydration state of BQ-BO and BQ-Py polymers was analyzed using THz-TDS (Fig. 8g). THz-TDS is used to analyze the hydration state, including water weakly affected by solutes, and the method was applied to study the hydration behavior of macromolecules and small molecules.[73–84] In the THz frequency band, there exists collective rotational relaxation dynamics of water (slow relaxation), dynamics of water isolated from hydrogen bonds (fast relaxation), and stretching vibrations between water molecules.[85–87] Hydration amount were obtained with the same method in literatures.[75,77,81,82] When water is bound to a solute, the slow relaxation becomes slower than the bulk water, and the intensity of the slow relaxation of the bulk water is reduced by the decrease in the amount of bulk water. Primarily, the amount of hydration water can be quantified from this decrease in bulk water. Since the amount of fast relaxation also changes slightly, we assume that slow relaxation and fast relaxation are independent and added this change to the hydration amount. The spectrum shown in Fig. 8g was fitted with the following eqn (2),[75–77] and obtained parameters were used to calculate the amount of hydration n from eqn (3).[74] Because of the accuracy of the measurement, only the imaginary part was used in the analysis.

$$\tilde{\varepsilon}(\omega) = c\left(\frac{\Delta\varepsilon_{\mathrm{slow}}}{1+i\omega\tau_{\mathrm{slow}}} + \frac{\Delta\varepsilon_{\mathrm{fast}}}{1+i\omega\tau_{\mathrm{fast}}} + \frac{A_{\mathrm{s}}}{\omega_{\mathrm{s}}^2-\omega^2+i\omega\gamma_{\mathrm{s}}}\right). \quad (2)$$

$$n = N\left(\frac{\frac{\Delta\varepsilon_{\mathrm{slow}}^{\mathrm{water}}-\Delta\varepsilon_{\mathrm{slow}}^{\mathrm{solution}}}{g_{\mathrm{slow}}} - \frac{\Delta\varepsilon_{\mathrm{fast}}^{\mathrm{solution}}-\Delta\varepsilon_{\mathrm{fast}}^{\mathrm{water}}}{g_{fast}}}{\frac{\Delta\varepsilon_{\mathrm{slow}}^{\mathrm{water}}}{g_{\mathrm{slow}}}+\frac{\Delta\varepsilon_{\mathrm{fast}}^{\mathrm{water}}}{g_{\mathrm{fast}}}}\right) \quad (3)$$

where $\Delta\varepsilon_{\mathrm{slow}}$ and $\Delta\varepsilon_{\mathrm{fast}}$ are the strengths of slow and fast relaxation, τ_{slow} and τ_{fast} are their relaxation times, respectively. The third term in the parentheses indicates the intermolecular stretching vibration between the water molecules. A_{s}, ω_{s}, and γ_{s} are the amplitude, angular frequency, and damping constant, respectively, and c represents the volume fraction of water in the system. The weight fraction was used as an approximation of the volume fraction. The superscripts "water" and "solution" in eqn (3) denote the results of pure water and solutions, respectively. N is the total weight of water per unit weight of solute in the solution. g_{slow}=2.9 and g_{fast}=1.0 are Kirkwood's correlation factors for slow and fast relaxation, respectively.[79] As the solution contains not only BQ-BO or BQ-Py but also NaOH, the effect of hydration by NaOH was subtracted after calculating the total hydration of the solution. Thus, the results for NaOH solution are also displayed in Fig. 8g. The spectrum was higher in NaOH solution than in pure water, indicating negative hydration.[88] The calculated amount of the hydrated water was $n = 1.55$ g for 1 g BQ-BO and $n = 2.48$ g for 1 g BQ-Py. The details of the calculation procedure were summarized in Supporting Information. The results imply that the amorphous conjugated polymer networks have the specific affinity to water molecules compared with the conventional carbon materials, even though the polymer is comprised of the rigid conjugated moiety. Moreover, the BQ-based conjugated polymers can be regarded as a new family of aquatic functional materials.

Conclusions

The present work showed the potentials of amorphous conjugated polymer networks for energy-related applications, such as electrocatalysts for HER. Prior to the molecular design and synthesis, a straightforward prediction model of metal-free HER electrocatalysts was constructed on small data based on the literatures using SpM-S. The Δ*E* predictor facilitates the molecular design of the high-performance catalysts. Based on the prediction, a couple of furane derivatives were selected as the monomer for the polymerization with BQ. The BQ-BO amorphous conjugated polymer network was obtained by microwave-assisted synthesis at 200 °C. After the dispersion in an organic medium, the resultant BQ-BO polymer with both the bulk and nanoparticles showed Δ*E* = 230 mV, which is one of the highest performances in the metal-free electrocatalysts synthesized lower than 200 °C. Metal-free HER catalysts alternative to Pt can be designed based on the present results. We found that BQ-BO and BQ-Py had the specific hydration state compared with the other nanocarbons. Amorphous conjugated polymer network with the enhanced performances can be designed and synthesized based on the prediction model.

Conflicts of interest

There are no conflicts to declare.

Acknowledgements

This work was supported by JSPS-KAKENHI (JP19H05717 to M. H., JP22H04559 to Y. O.) and Toray Science Foundation (Y.O.).

Notes and references

1 M. Eddaoudi, D. B. Moler, H. Li, B. Chen, T. M. Reineke, M. O'Keeffe and O. M. Yaghi, *Acc. Chem. Res.*, 2001, **34**, 319.
2 C. Weder, *Chem. Commun.*, 2005, 5378.
3 X. Feng, X. Ding nd D. Jiang, *Chem. Soc. Rev.*, 2012, **41**, 6010.
4 J. S. M. Lee, A. I. Cooper, *Chem. Rev.*, 2020, **120**, 2171.
5 X. Feng and D. A. Schlüter, *Angew. Chem. Int. Ed.*, 2018, **57**, 13748.
6 T. Kato, J. Uchida, T. Ichikawa and T. Sakamoto, *Angew. Chem. Int. Ed.*, 2018, **57**, 4355.
7 D. Chen, C. Liu, J. Tang, L. Luo and G. Yu, *Polym. Chem.*, 2019, **10**, 1168.

8 E. A. Neal and T. Nakanishi, *Bull. Chem. Soc. Jpn.*, 2021, **94**, 1769.
9 K. Ariga, *Nanoscale*, 2022, **14**, 10610.
10 J. Suzuki, A. Ishizone, K. Sato, H. Imai, Y. J. Tseng, C. H. Peng and Y. Oaki, *Chem. Sci.*, 2020, **11**, 7003.
11 S. Yano, K. Sato, J. Suzuki, H. Imai and Y. Oaki, *Commun. Chem.*, 2019, **2**, 97.
12 Y. Oaki and K. Sato, *Nanoscale Adv.*, 2022, **4**, 2773.
13 S. Curtarolo, G. L. W. Hart, M. B. Nardelli, N. Mingo, S. Sanvito and O. Levy, *Nat. Mater.*, 2013, **12**, 191.
14 K. T. Butler, J. M. Frost, J. M. Skelton, K. L. Svanea and A. Walsh, *Chem. Soc. Rev.*, 2016, **45**, 6138.
15 B. Sanchez-Lengeling and A. Aspuru-Guzik, *Science*, 2018, **361**, 360.
16 L. Himanen, A. Geurts, A. S. Foster and P. Rinke, *Adv. Sci.*, 2019, **6**, 1900808.
17 J. A. Keith, V. Vassilev-Galindo, B. Cheng, S. Cheiela, M. Gastegger, K. R. Muller and A. Tkatchenko, *Chem. Rev.*, 2021, **121**, 9816.
18 A. Aspuru-Guzik, *Digital Discovery*, 2022, **1**, 6.
19 E. Ren, P. Guilbaud and F. X. Coudert, *Digital Discovery*, 2022, **1**, 355.
20 K. Hatakeyama-Sato, *Polym. J.*, 2023, **55**, 117.
21 S. Zhu, K. Jiang, B. Chen and S. Zheng, *J. Mater. Chem. A*, 2023, **11**, 3849.
22 Y. Oaki and Y. Igarashi, *Bull. Chem. Soc. Jpn.*, 2021, **94**, 2410.
23 R. Mizuguchi, Y. Igarashi, H. Imai and Y. Oaki, *Nanoscale*, 2021, **13**, 3853.
24 Y. Haraguchi, Y. Igarashi, H. Imai and Y. Oaki, *Digital Discovery*, 2022, **1**, 26.
25 T. Komura, K. Sakano, Y. Igarashi, H. Numazawa, H. Imai and Y. Oaki, *ACS Appl. Energy Mater.*, 2022, **5**, 8990.
26 K. Sakano, Y. Igarashi, H. Imai, S. Miyakawa, T. Saito, Y. Takayanagi, K. Nishiyama and Y. Oaki, *ACS Appl. Energy Mater.*, 2022, **5**, 2074.
27 H. Tobita, Y. Namiuchi, T. Komura, H. Imai, K. Obinata, M. Okada, Y. Igarashi and Y. Oaki, *Energy Adv.*, 2023, **2**, 1014.
28 J. Greelye, T. F. Jaramillo, J. Bonde, I, Chorkendorff and J. K. Nørskov, *Nat. Mater.*, 2006, **5**, 909.
29 J. Duan, S. Chen, M. Jaroniec and S. Z. Qiao, *ACS Catal.*, 2015, **5**, 5207.
30 W. Zhou, J. Jia, J. Lu, L. Yang, D. Hou, G. Li and S. Chen, *Nano Energy*, 2016, **28**, 29.
31 J. Zhang, G. Chen, K. Müllen and X. Feng, *Adv. Mater.*, 2018, **30**, 1800528.
32 H. Huang, M. Yan, C. Yang, H. He, Q. Jiang, L. Yang, Z. Lu, Z. Sun, X. Xu, Y. Bando and Y. Yamauchi, *Adv. Mater.*, 2019, **31**, 1903415.
33 T. Li, T. Hu, L. Dai and C. M. Li, *J. Mater. Chem. A*, 2020, **8**, 23674.
34 Y. Deng, Y. Wang, Y. Chen and Z. Zhang, *Chem. Asian J.*, 2021, **16**, 1851.
35 D. H. Yang, Y. Tao, X. Ding and B. H. Han, *Chem. Soc. Rev.*, 2022, **51**, 761.
36 Y. Ito, C. Weitao, T. Fujita, Z. Tang and M. Chen, *Angew. Chem. Int. Ed.*, 2015, **54**, 2131.
37 B. Deng, D. Wang, Z. Jiang, J. Zhang, S. Shi, Z. Jiang and M. Liu, Carbon, 2018, **138**, 169.
38 Y. Ito, Y. H. Shen, D. Hojo, Y. Itagaki, T. Fujita, L. H. Chen, T. Aida, Z. Tang, T. Adschiri and M. W. Chen, *Adv. Mater.*, 2016, **28**, 10644.
39 J. Zhou, F. Qi, Y. Chen, Z. Wang, B. Zheng and X. Wang, *J. Mater. Sci.*, 2018, **53**, 7767.
40 Y. Zheng, Y. Jiao, Y. Zhu, L. H. Li, Y. Han, Y. Chen, A. Du, M. Jaroniec and S. Z. Qiao, *Nat. Commun.*, 2014, 5, 3783.
41 Y. Zhao, F. Zhao, X. Wang, C. Xu, Z. Zhang, G. Shi and L. Qu, *Angew. Chem. Int. Ed.*, 2014, **53**, 13934.
42 X. Liu, M. Zhang, D. Yu, T. Li, M. Wan, H. Zhu, M. Du and J. Yao, *Electrochim. Acta*, 2016, **215**, 223–230.
43 J. Duan, S. Chen, M. Jaroniec and S. Z. Qiao, *ACS Nano*, 2015, **9**, 931.
44 L. Wei, H. E. Karahan, K. Goh, W. Jiang, D. Yu, O. Birer, R. Jiang and Y. *J. Chen, Mater. A*, 2015, **3**, 7210.
45 L. Chen, J. Han, Y. Ito, T. Fujita, G. Huang, K. Hu, A. Hirata, K. Watanabe, M. Chen, *Angew. Chem. Int. Ed.*, 2018, **57**, 13302.
46 N. Wei, Q. Li, S. Cong, H. Ci, Y. Song, Q. Yang, C. Lu, C. Li, G. Zou, J. Sun, Y. Zhang and Z. Liu, *J. Mater. Chem. A.*, 2019, **7**, 4813.
47 S. Suragtkhuu, M. Bat-Erdene, A. S. R. Bati, J. G. Shapter, S. Davaasambuu and M. Batmunkh, *J. Mater. Chem. A*, 2020, **8**, 20446.
48 Q. Hanniet, M. Boussmen, J. Bares, V. Huon, I. Iatsunskyi, E. Coy, M. Bechelany, C. Gervais, D. Voiry, P. Miele and C. Salameh, *Sci. Rep.*, 2020, **10**, 22003.
49 Z. Xu, Q. Zhang, M. Li, F. Luo, Y. Liu, R. Wang, X. Ma, Z. Yang and D. Zhang, *ChemCatChem*, 2020, **12**, 5543.
50 D. Yan, S. Dou, L. Tao, Z. Liu, Z, Liu J. Huo and S. Wang, *J. Mater. Chem. A*, 2016, **4**, 13726-13730.
51 S. N. Talapaneni, J. Kim, S. H. Je, O. Buyukcakir, J. Oh and A. Coskun, *J. Mater. Chem. A*, 2017, **5**, 12080.
52 W. Cui, Q. Liu, N. Cheng, A. M. Asiri and X. Sun, *Chem. Commun.*, 2014, **50**, 9340.
53 Y. Tian, Y. Ye, Y. Wang, S. Peng, Z. Wei, X. Zhang and W. Liu, *Appl. Catal. A*, 2016, **4**, 12205.
54 A. Mulyadi, Z. Zhang, M. Dutzer, W. Liu and Y. Deng, *Nano Energy*, 2017, **32**, 336-346.
55 D. Wu, Q. Xu, J. Qian, X. Li and Y. Sun, *Chem. Eur. J.*, 2019, **25**, 3105.
56 D. Zhou, X. Tan, H. Wu, L. Tian and M. Li, *Angew. Chem. Int. Ed.*, 2019, **58**, 1376.
57 L. Hui, Y. Xue, Y. Liu and Y. Li, *Small*, 2021, **17**, 2006136/
58 S. Ruidas, B. Mohanty, P. Bhanja, E. S. Erakulan, R. Thapa, P. Das, A. Chowdhury, S. K. Mandal, B. K. Jena, A. Bhaumik, *ChemSusChem*, 2021, **14**, 5057.
59 H. Coskun, A. Aljabour, P. de Luna, H. Sun, N. Nishiumi, T. Yoshida, G. Koller, M. G. Ramsey, T. Greunz, D. Stifter, M. Strobel, S. Hild, A. W. Hassel, N. S. Sariciftci, E. H. Sargent and P. Stadler, *Adv. Mater.*, 2020, **32**, 1902177.
60 M. Chen and M. Li, *Chem. Eur. J.*, 2019, **25**, 13860.
61 B. C. Patra, S. Khilari, R. N. Manna, S. Mondal, D. Pradhan, A. Pradhan and A. Bhaumik, *ACS Catal.*, 2017, **7**, 6120.
62 H. Tabassum, R. Zou, A. Mahmood, Z. Liang and S. Guo, *J. Mater. Chem. A*, 2016, **4**, 16469.
63 H. S. Jena, C. Krishnaraj, S. Parwaiz, F. Lecoeuvre, J. Schmidt, D. Pradhan and P. V. D. Voort, *ACS Appl. Mater. Interfaces*, 2020, **12**, 44689.
64 Y. Ma, Y. Fu, W. Jiang, Y. Wu, C. Liu, G. Che and Q. Fang, J. *Mater. Chem. A* 2022, **18**, 10092.
65 M. Cheng and M. Li, *Chem. Eur. J.*, 2019, **25**, 13860.
66 W. Wang, Y. Zhang, L. Chen, H. Chen, S. Hu, O. Li, H. Liu and S. Qiao, *Polym. Chem.*, 2021, **12**, 650.
67 A. Pradhan and R. N. Manna, *ACS Appl. Polym. Mater.*, 2021, **3**, 1376.
68 R. Sakamoto, R. Shiotsuki, K. Wada, N. Fukui, H. Maeda, J. Komeda, R. Sekine, K. Harano and H. Nishihara, *J. Mater. Chem. A*., 2018, **8**, 22189.
69 S. S. Shinde, A. Sami and J. H. Lee, *ChemCatChem*, 2015, **7**, 3873.
70 J. K. Nørskov, T. Bligaard, A. Logadottir, J. R. Kitchin, J. G. Chen, S. Pandelov and U. Stimming, *J. Electrochem. Soc.*, 2005, **153**, 323.
71 J. Greeley, T. F. Jarmillo, J. Bonde, I. Chorkendorff and J. K. Nørskov, *Nat. Mater.*, 2006, **5**, 909.
72 Y. Zheng, Y. Jiao, L. H. Li, T. Xing, Y. Chen, M. Jaroniec, S. Z. Qiao, *ACS Nano*, 2014, **8**, 5290.

73 M. Hishida and K. Tanaka, *Phys. Rev. Lett.*, 2011, **106**, 158102.
74 M. Hishida and K. Tanaka, *J. Phys. Condens. Matter.*, 2012, **24**, 284113.
75 M. Hishida, R. Anjum, T. Anada, D. Murakami and M. Tanaka, *J. Phys. Chem. B*, 2022, **126**, 2466.
76 M. Hishida, K. Tanaka, Y. Yamamura and K. Saito, *J. Phys. Soc. Jpn.*, 2014, **83**, 044801.
77 M. Hishida, A. Kaneko, Y. Yamamura and K. Saito, *J. Phys. Chem. B*, 2023, **127**, 6296.
78 T. Arikawa, M. Nagai and K. Tanaka, *Chem. Phys. Lett.*, 2008, **457**, 12.
79 K. Shiraga, Y. Ogawa, K. Tanaka, T. Arikawa, N. Yoshikawa, M. Nakamura, K. Ajito and T. Tajima, *J. Phys. Chem. B*, 2018, **122**, 1268.
80 N. V. Penkov, *Biophys. Rev.*, 2023, *15*, 833.
81 T. Tominaga, M. Hishida, D. Murakami, Y. Fujii, M. Tanaka and H. Seto, *J. Phys. Chem. B*, 2022, **126**, 1758.
82 M. Hishida, R. Kanno and T. Terashima, *Macromolecules*, 2023, **56**, 7587.
83 K. Shiraga, Y. Ogawa and N. Kondo, *Biophys. J.*, 2016, **111**, 2629.
84 J. Sugiyama, Y. Tokunaga, M. Hishida, M. Tanaka, K. Takeuchi, D. Satoh and M. Imashimizu, *Nat. Commun.*, 2023, **14**, 2825.
85 C. Rønne, P.-O. Åstrand and S. R. Keiding, *Phys. Rev. Lett.*, 1999, **82**, 2888.
86 K. Shiraga, K. Tanaka, T. Arikawa, S. Saito and Y. Ogawa, *Phys. Chem. Chem. Phys*., 2018, **20**, 26200.
87 H. Yada, M. Nagai and K. Tanaka, *Chem. Phys. Lett*., 2008, **464**, 166.
88 G. Engel and H. G. Hertz, *Berichte Bunsenges. Für Phys. Chem*., 1968, **72**, 808.